SpaceOps-2025, ID # 162

Orientation-Based Collision Avoidance Maneuver (OCAM) of Satellites

Farhad Aghili[a]*

[a] *Canadian Space Agency (CSA), 6767 route de l'aeroport, St-Hubert, Quebec, J3Y 8Y9, Canada*
* Corresponding Author

Abstract

Aerodynamic drag and solar radiation pressure (SRP) are the primary natural forces acting on satellites in intermediate orbits. While significantly weaker than thruster-generated forces, they act continuously rather than impulsively. Given sufficient lead time before the time of closest approach (TCA), these continuous perturbations can alter a satellite's trajectory enough to reduce collision risk, enabling propulsion-less collision avoidance. This paper explores the feasibility of leveraging controlled aerodynamic drag and SRP for propulsion-less collision avoidance. The proposed *Orientation-based Collision Avoidance Maneuver* (OCAM) optimizes the satellite's orientation to maximize the miss distance between the primary and secondary objects while minimizing the probability of collision. This approach exploits the combined effects of SRP and drag forces, where drag-induced acceleration depends on the exposed effective surface area, and SRP-induced acceleration accounts for sun-exposed surfaces modeled as a blackbody absorber, specular reflector, and Lambertian diffuser. The maneuver's effectiveness is evaluated by computing the resulting miss distance and collision probability based on these continuous perturbation forces. The control algorithm requires the following inputs: Conjunction data, including TLEs for the primary and secondary objects from the CDM alert; Cross-sectional areas of the primary satellite, including the mean cross-sectional area normal to the in-track direction prior to the CDM alert; Reflectivity coefficients of the primary satellite's surfaces, including specular and diffuse reflection properties; The atmospheric drag coefficient, derived from solar activity-based atmospheric mass density look-up tables or energy dissipation rate estimations typically provided in the CDM. Case studies are presented to assess the effectiveness of OCAM in enabling propulsion-less satellites to perform collision avoidance maneuvers.

Keywords: satellite collision avoidance, aerodynamics drag, solar radiation pressure, orbital mechanics, spacecraft control

Acronyms/Abbreviations

AU	Astronomical Unit (distance between the Earth and the Sun approximately 149.6 million km).
COLA	Collision avoidance.
CDM	Conjunction Summary Message.
OCAM	Orientation-Based Collision Avoidance Maneuver.
NEOSSat	Near-Earth Object Surveillance Satellite.
18 SDS	18th Space Defense Squadron.
TCA	Time of closest approach.
SRP	Solar radiation pressure.
RTN	Radial-Tangential-Normal frame (a local reference frame used in orbital mechanics).
POC	Probability of collision.

Nomenclature

$\mathbf{a}_{\text{drg}}, \mathbf{a}_{\text{srp}}$	=	Satellite acceleration due to atmospheric drag and solar radiation pressure.
A_k^*, A_k	=	The exposed and actual areas of the *k*-th surface of the satellite.
c_d	=	Drag coefficient.
d	=	Energy dissipation rate per mass.
$\dot{e}$	=	Power dissipation due to drag.
m	=	Satellite mass.
$\mathbf{n}_k$	=	Unit vector perpendicular to to the *k*-th surface of the satellite.
$\mathbf{v}$	=	Satellite velocity vector.

ρ	=	Atmospheric density.
ω	=	Orbit angular velocity.
h	=	Satellite altitude above the Earth's surface.
P_c	=	Probability of collision.
p	=	Solar radiation pressure at 1 AU.
$\mathbf{r}_{\text{miss}}$, $\mathbf{r}^{+}_{\text{miss}}$	=	Miss distance before and after the maneuver.
$\mathbf{q}$	=	Quaternion representing satellite orientation.
$t2\text{tca}$	=	Time to TCA.
$\mathbf{Q}$	=	Covariance matrix of the position vector.
$\mathbf{s}$	=	The sun unit vector.
ϱ_k , δ_k	=	The specular and diffuse reflectivity coefficients of *k*-th surface of the satellite.

1. Introduction

The increasing number of both operational and defunct satellites, along with space debris, poses a growing risk of collision, threatening the safety of active space assets. As a result, the ability of satellites to execute collision avoidance (COLA) maneuver is crucial—not only for protecting spacecraft in orbit but also for ensuring the long-term sustainability of the space environment. Without effective mitigation strategies, collisions can trigger a cascading effect known as the Kessler syndrome [1], in which debris from one collision leads to further collisions, exponentially increasing the amount of space debris.

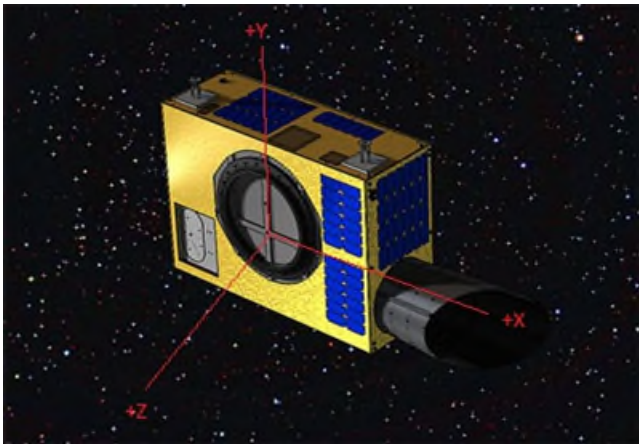

Figure 1: Artistic rendering of NEOSSat in sun-synchronous orbit, subject to solar radiation and drag.

To mitigate this risk, organizations such as the 18th Space Defense Squadron (18 SDS) issue collision alerts by tracking satellites and space debris larger than 10 cm [2]. When a potential conjunction is detected, satellites equipped with propulsion systems can adjust their trajectories using COLA manuvers. These maneuvers rely on impulsive thrust to increase the miss distance and reduce the probability of collision [3]. From an operational standpoint, a collision risk assessment and mitigation system is essential for satellite safety. Such systems process a CDM (Conjunction Summary Message) from sources like 18 SDS and determine whether a COLA manuever is necessary, planning and executing maneuvers when a high-probability conjunction is identified. If a satellite has an onboard impulsive or continuous propulsion system, a burn can be carefully planned to maximize the miss distance while minimizing the probability of collision, ensuring compliance with predefined safety thresholds [12,13]. At the same time, these maneuvers must satisfy operational constraints such as minimizing propellant consumption. However, many small satellites lack onboard propulsion, necessitating alternative collision avoidance strategies. In such cases, satellites can exploit naturally occurring orbital perturbations, such as aerodynamic drag and solar radiation pressure (SRP), to modify their orbits [4,5,6,7].

In low Earth orbit (LEO), aerodynamic drag is the dominant perturbation force, while SRP becomes more significant at higher altitudes. In intermediate orbits, both forces contribute to orbital perturbations. Although these forces are considerably weaker than thruster-generated impulses, they act continuously rather than instantaneously. Given sufficient lead time before the time of closest approach (TCA), these continuous perturbations can gradually alter a satellite's trajectory enough to mitigate collision risk, enabling propulsion-less collision avoidance maneuvers.

This paper explores the feasibility of using controlled aerodynamic drag and solar radiation pressure (SRP) to enable collision avoidance maneuvers for satellites without an onboard propulsion system, such as NEOSSat—a Canadian microsatellite equipped with a 15 cm aperture f/5.88 Maksutov telescope, similar to the one on the MOST spacecraft [16] (see Figure 1). First, a model is developed to characterize perturbation accelerations due to drag and solar radiation as functions of the satellite's orientation. The drag-induced acceleration accounts for exposed effective surface areas, while the SRP-induced acceleration considers the sun-exposed surfaces, modeled as a combination of a blackbody absorber, a specular reflector, and a Lambertian diffuser. Next, the resulting miss distance and probability of collision are calculated based on the continuous perturbation forces. Finally, case studies are presented to evaluate the effectiveness of this approach in performing collision avoidance maneuvers for propulsion-less satellites.

2. COLA Based on Drag and Solar Radiation

2.1 Modelling Orbit Acceleration Due to Drag and Solar Radiation

Figure 2 shows a schematic of a satellite in Earth orbit under the influence of drag and SRP perturbations, expressed in the Radial–Tangential–Normal (RTN) frame. The theoretical model for computing satellite drag is formulated as:

$$\mathbf{a}_{\text{drg}} = -\frac{1}{2}\frac{c_d\rho}{m}\sum_k A_k^* \parallel \mathbf{v} \parallel \mathbf{v} \tag{1}$$

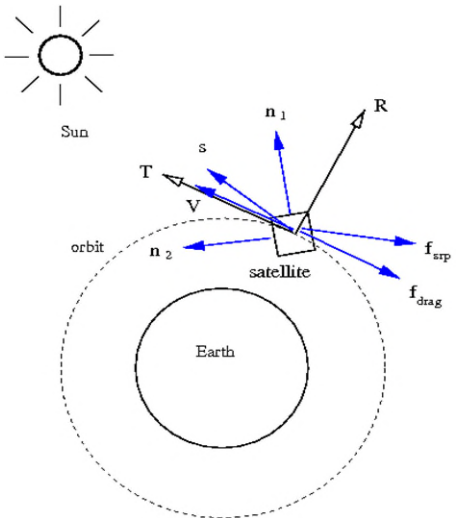

Figure 2: A Satellite subjected to drag and SRP perturbations.

where $\mathbf{a}_{\text{drg}}$ represents the drag-induced acceleration in the Radial-Tangential-Normal (RTN) coordinate frame, ρ denotes atmospheric density, m is the spacecraft mass, and c_d is the drag coefficient. The velocity vector $\mathbf{v}$ characterizes the spacecraft's motion relative to the atmosphere. The summation accounts for contributions from each satellite surface indexed by k, where A_k^* denotes the exposed effective surface area. It should be noted that in model (1) neglects atmospheric winds and thus the relative velocity is assumed to be equal to the satellite's orbital velocity. Moreover, the lift coefficients are typically much smaller than the corresponding drag coefficients; therefore, perturbing lift forces are not considered here. Let $\mathbf{n}_k$ denote the unit normal vector associated with the k-th surface. Then, the effective surface area can be related to the actual surface area A_k by the cosine of the angle between the normal vector and the velocity vector, i.e., $A_k^* = A_k(\mathbf{n}_k \cdot \mathbf{v}/\parallel \mathbf{v} \parallel)$. Thus, (1) can be equivalently rewritten as:

$$\mathbf{a}_{\text{drg}} = -\frac{1}{2}\frac{c_d\rho}{m}\sum_k A_k(\mathbf{n}_k \cdot \mathbf{v})\mathbf{v}. \tag{2}$$

Notably, vector $\mathbf{n}_k$ is a function of the spacecraft's attitude. Given the quaternion $\mathbf{q} = [\mathbf{q}_v^T \ q_o]^T$, which represents the orientation of the spacecraft's body-fixed frame relative to the RTN frame, the surface normal vectors are given by:

$$\mathbf{n}_k(\mathbf{q}) = (\mathbf{I} + 2q_o[\mathbf{q}_v \times] + 2[\mathbf{q}_v \times]^2)\mathbf{b}_k, \tag{3}$$

where $\mathbf{b}_k$ represents the fixed unit normal vector in the spacecraft's body frame, and $[\cdot\times]$ represents the matrix form of the cross product. The drag coefficient for medium-class satellites typically ranges from 2.0 to 2.5; thus, a nominal value of $c_d = 2.25$ is adopted for computational purposes. For a primary spacecraft in a circular orbit, the velocity vector aligns with the in-track direction and has a magnitude given by:

$$v = \parallel \mathbf{v} \parallel = \omega(R_e + h), \tag{4}$$

where $R_e = 6.371 \times 10^6$ m represents Earth's mean radius, h is the spacecraft altitude above the Earth's surface, and ω is the orbital angular velocity

$$\omega = \sqrt{\frac{\mu}{(R_e+h)^3}}. \tag{5}$$

Here $\mu = 3.986 \times 10^{14}$ m ^{3}/s ^{2} is Earth's gravitational parameter.

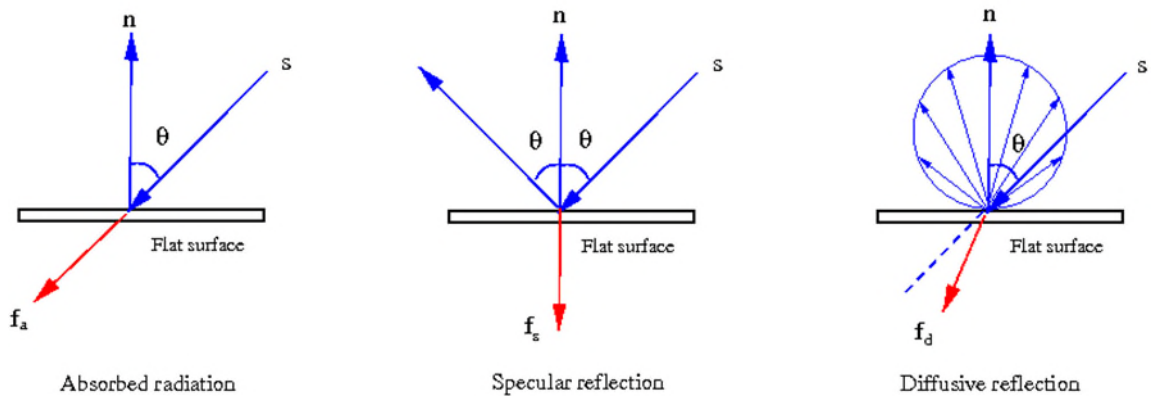

Figure 3: The SRP force vector acting on a flat surface with three distinct combinations of reflectivity and absorptivity.

Figure 3 shows the resulting SRP force on a flat surface as the sum of contributions from absorbed radiation, specular reflection, and diffuse reflection [8,9]. The perturbation acceleration due to solar radiation pressure (SRP) is modeled under the assumption that each satellite surface behaves as a composite of a blackbody absorber, a specular reflector, and a Lambertian diffuser [8,9]. The resulting SRP-induced acceleration is given by:

$$\mathbf{a}_{\text{srp}} = -\frac{c_r p}{m}\sum_{k=1} A_k \mathbf{s}^T \mathbf{n}_k \left((1-\varrho_k)\mathbf{s} + 2\left(\varrho_k \mathbf{s}^T \mathbf{n}_k + \frac{1}{3}\delta_k\right)\mathbf{n}_k\right), \tag{6}$$

where each surface is characterized by specular and diffuse reflectivity coefficients, ϱ_k and δ_k, respectively. The sun unit vector is denoted as $\mathbf{s}$, $p = 4.56 \times 10^{-6}$ N/m ^{2} represents the nominal solar radiation pressure at 1 AU., and the dimensionless scale factor c_r is introduced with a nominal value of unity.

2.2 Orientaiton-based COLA Manuever

Now, we are ready to incorporate the models of drag and SRP perturbations to enable a collision avoidance maneuver. Note that both drag and SRP acceleration perturbations described in (2) and (6) are orientation-dependent due to their reliance on (3). Suppose the orientation of the primary spacecraft changes from $\mathbf{q}$ to $\mathbf{q}^+$. The resulting net perturbation due to this change in orientation is: $\mathbf{a}_{pert} = \mathbf{a}_{\text{drg}}(\mathbf{q}^+) + \mathbf{a}_{\text{srp}}(\mathbf{q}^+) - \mathbf{a}_{\text{drg}}(\mathbf{q}) - \mathbf{a}_{\text{srp}}(\mathbf{q})$. The relative motion of a secondary object with respect to the primary spacecraft is encapsulated by the state vector:

$$\mathbf{x}^T = [\delta\mathbf{r}^T \; \delta\dot{\mathbf{r}}^T], \tag{7}$$

where $\delta\mathbf{r}$ and $\delta\dot{\mathbf{r}}$ denote position and velocity changes. The time evolution of relative motion under perturbative effects follows the Clohessy–Wiltshire (CW) equations [10, 11]:

$$\frac{d}{dt}\mathbf{x} = \mathbf{A}\mathbf{x} + \mathbf{b}u(t), \quad \text{where} \quad \mathbf{A} = \begin{bmatrix} \mathbf{0} & \mathbf{I} \\ \mathbf{L}(\omega) & -2[\boldsymbol{\omega}\times] \end{bmatrix}, \tag{8}$$

with $\mathbf{L}(\omega) = \text{diag}\,(3\omega^2, 0, -\omega^2)$, $\mathbf{b}^T = [\mathbf{0} \;\; \mathbf{a}_{pert}^T]$, and $u(t)$ as the unit pulse function. The system response at the Time of Closest Approach (TCA), denoted as $t2tca$, is obtained via convolution:

$$\mathbf{x}(t2\text{tca}) = \int_0^{t2\text{tca}} e^{\mathbf{A}(t-\tau)}\mathbf{b}u(\tau)d\tau. \tag{9}$$

The convolution integral above can be solved to yield the miss-distance variation in the following closed-form expression:

$$\delta\mathbf{r} = \begin{bmatrix} 1-\cos(\omega t_{t2\text{tca}}) & 2\omega t_{t2tca} - 2\sin(\omega t_{t2tca}) & 0 \\ 2\sin(\omega t_{t2\text{tca}}) - 2\omega t_{t2\text{tca}} & 4 - \frac{3}{2}\omega^2 t_{t2\text{tca}}^2 - 4\cos(\omega t_{t2\text{tca}}) & 0 \\ 0 & 0 & 1-\cos(\omega t_{t2\text{tca}}) \end{bmatrix} \frac{\mathbf{a}_{\text{pert}}}{\omega^2} \tag{10}$$

Updating the predicted miss distance, we obtain:

$$\mathbf{r}_{miss}^{+} = \mathbf{r}_{miss} + \delta\mathbf{r}, \tag{11}$$

where $\mathbf{r}_{miss}$ and $\mathbf{r}_{miss}^{+}$ represent the miss-distances before and after the collision avoidance maneuver. The revised probability of collision is then computed from the covariances of the position vectors of the primary and secondary satellites in the new miss distance calculated in (11). It has also been demonstrated that the covariances associated with the position vectors of the primary and secondary satellites can be combined into a new covariance matrix within the encounter plane [14,15], expressed as follows:

$$\mathbf{\Sigma} = \begin{bmatrix} \sigma_x^2 & \kappa\sigma_x\sigma_z \\ \kappa\sigma_x\sigma_z & \sigma_z^2 \end{bmatrix}. \tag{12}$$

Denoting R_c as the combined hard-body radius of the primary and secondary objects, the probability of collision P can then be approximated by [14, 15]:

$$P_c = \frac{R_c^2}{2\sigma_x\sigma_{zeq}} \exp\left(-\frac{\|\mathbf{r}_{miss}^{+}\|^2}{2\sigma_{zeq}^2}\right), \tag{13}$$

where $\sigma_{zeq} = \sigma_z\sqrt{1-\kappa^2}$ represents the equivalent position error in z-direction with zero correlation [14].

2.3 Estimation of Atmospheric Density from Power Dissipation

The accuracy of drag force estimation at high altitudes critically depends on precise knowledge of atmospheric density, which varies significantly with solar and geomagnetic activity. Empirical models, such as MSISE [19], serve as essential tools for predicting these variations. Alternatively, atmospheric density can be inferred from Conjunction Data Messages (CDMs), which occasionally provide information such as energy dissipation per unit mass. Since the dissipation energy rate $\dot{e}$ is associated with drag, it can be inferred that

$$\dot{e} = \frac{1}{2} c_d \rho \sum_k A_k^* \, \| \mathbf{v} \|^3 \tag{14}$$

The above equation can be used to estimate atmospheric density as follows:

$$\rho = \frac{2d}{c_b \, \| \mathbf{v} \|^3}$$

where $d = \dot{e}/m$ is the dissipation energy per mass and $c_b = m/(c_d \sum_k A_k^*)$ is the ballistic coefficient.

2.4 Comparison of Drag and Radiation Pressure

Figure 4 illustrates the pressure due to drag and solar radiation pressure (SRP) as a function of altitude for different levels of solar activity: low, medium, and high. It should be noted that atmospheric density is strongly correlated with solar activity, which in turn affects drag pressure. For this comparison, the drag and solar radiation pressure coefficients are taken as 2.2 and 1.0, respectively. The plots clearly show that at low altitudes, drag pressure dominates and decreases almost exponentially with altitude, whereas SRP remains nearly constant since altitude has a negligible effect compared to the distance to the Sun. Based on the plots, SRP exceeds drag in the following scenarios: i) Beyond an altitude of 420 km during periods of low solar activity; ii) Beyond an altitude of 580 km during periods of medium solar activity; iii) Beyond an altitude of 900 km during periods of high solar activity. From the plots in the figure, one can conclude that at NEOSSat's altitude of 870 km, the pressure due to solar radiation dominates over drag, except under conditions of high solar and geomagnetic activity.

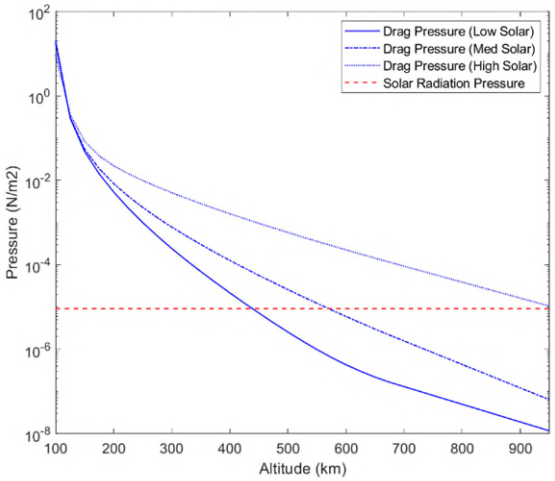

Figure 4: Comparison of drag and SRP pressures at different altitude.

3. Case Study

3.1 Operational Constraints

This section presents case studies demonstrating the application of the Orientation-based Collision Avoidance Maneuver (OCAM) to NEOSSat, a suitcase-sized microsatellite measuring 137 × 78 × 38 cm (including the telescope baffle) and weighing 74 kg. It operates in a sun-synchronous orbit with an inclination of approximately 98.6 degrees, a nearly circular trajectory (zero eccentricity), and an altitude of 780 km, completing one orbit every 100 minutes. NEOSSat's primary payload is a 15 cm aperture Maksutov optical telescope with a 0.86-degree field of view, equipped with two E2V 1024 × 1024 charge-coupled devices (CCDs) and associated readout electronics, providing a resolution of 3 arcseconds per pixel. One CCD is dedicated to scientific imaging, while the second functions as a specialized narrow-field star tracker, sharing the optical boresight and field of view [17]. The satellite's large baffle allows it to observe regions near the Sun, down to 45 degrees solar elongation—an area difficult to image with ground-based telescopes. The original Attitude Determination and Control System (ADCS) consists of: One three-axis magnetometer; Coarse sun sensing, derived from solar panel output on each face. Four reaction wheels with integrated range sensors (X,Y,Z,and Skew); Three torque rods; A custom narrow-field star tracker using the telescope boresight; two GPS receivers, mounted on the +Y and -Y faces. Together, the ADCS provides three-axis stabilization, achieving a pointing stability of 2 arcseconds during a 100-second exposure. It is important to note that specific operational constraints are applied during tracking to ensure the spacecraft's health [18]:

- The +X axis of NEOSSat's science detector is aligned with the target RSO.
- The -Z solar panel is oriented Sunward to maintain power and thermal constraints.
- The +Z instrument radiator is preferentially pointed toward deep space.

The line-of-sight constraints are:

- The RSO-centric solar phase angle must be less than 135 degrees.
- The grazing angle (RSO altitude above the Earth's limb) must be greater than 10 degrees.
- The lunar and planetary exclusion angles must be greater than 4 degrees.

3.2 Orientation Maneuvers in Orbit

We make the following assumptions for the OCAM analyis of NEOSSat: The orbital inclination is assumed to be 90 degree for simplicity (98 degree for the NEOSSat heliosynchronous orbit) and the Sun angle at any given point along the orbit remains constant throughout the year. Therefore, the Sun vector is aligned with the N-axis of the RTN orbital frame. NEOSSat is modeled as a rectangular shape with dimensions $1.37 \times 0.78 \times 0.38$ m and thus its baffle is ignored. Solar radiation pressure (SRP) due to Earth's albedo is neglected. Figure 5 illustrates NEOSSat in orbit under different principal orientation configurations. The base orientation configuration (Conf 0) is defined as the orientation where the NEOSSat XYZ local frame is aligned with the RTN frame, i.e., the roll angle $\theta = 0$. In this configuration, the force exerted on the spacecraft due to SRP acts entirely in the cross-track direction, meaning that SRP cannot induce significant drift due to the orbital plane's resistance to external perturbation forces. The drag force, acting on the XY ram side of the spacecraft, generates a force in the in-track direction, leading to drift in both in-track and radial directions. However, maximum drag force occurs in Configuration 1, where the roll angle is -90 degree. In this scenario, the spacecraft's maximum surface area (XY face) is exposed to atmospheric drag, making it the dominant cross-sectional area for drag forces. In this configuration, SRP effects remain negligible as the generated force is primarily in the cross-track direction. Configuration 2 is defined for roll angles between -90 and +90 degrees, where the force due to SRP has both cross-track and in-track components, allowing it to induce drift motion. In this case, drag acts on both XY and XZ surfaces, with the effective cross-sectional areas determined by the sine and cosine of the roll angle. Finally, Configuration 3 represents the minimum drag scenario, where the spacecraft's smallest surface area (YZ face) becomes the dominant drag cross-section. In this configuration, SRP remains inactive, as its force is directed solely in the out-track direction.

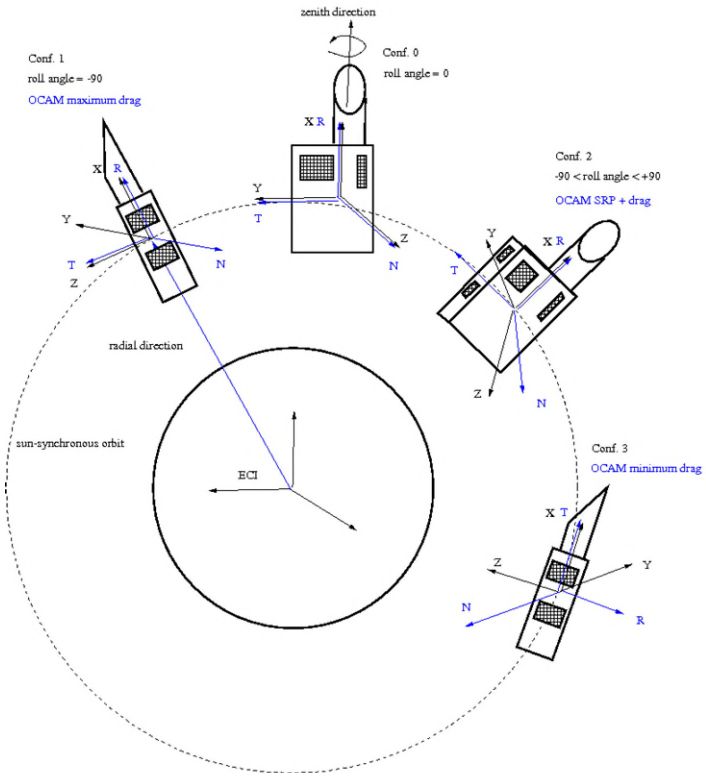

Figure 5: NEOSSat drag and SRP orientation manoeuvres in a sun synchronous orbit.

3.3 Analysis Results

This study investigates an orientation-based collision avoidance (COLA) maneuver for NEOSSat to mitigate conjunction risks with a secondary object under low to medium geomagnetic and solar activity conditions. In this case study, the secondary object is in conjunction with the primary satellite, with a miss distance of 30 m at the time of closest approach (TCA) and a collision probability of 26%. We aim to achieve a COLA maneuver by appropriately adjusting the primary satellite's orientation to increase the separation distance beyond the 1000 m threshold and to reduce the collision probability below the acceptable limit of 10^{-6}.

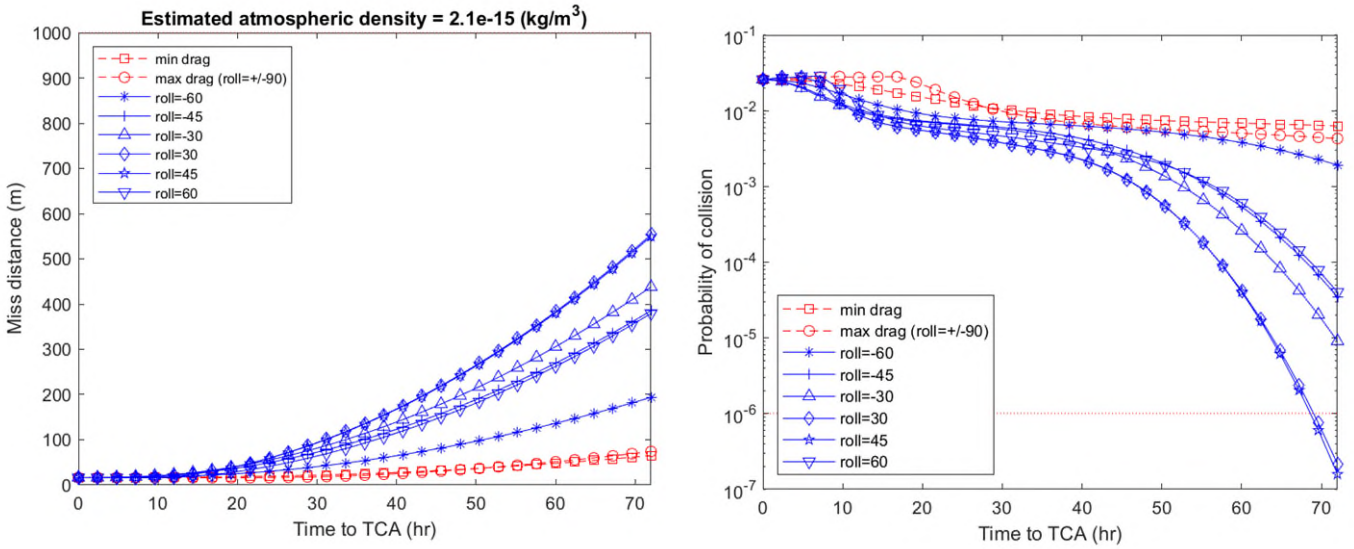

Figure 6: The miss-distance curves (left) and PoC curves (right) as functions of satellite orientation and time to TCA under low geomagnetic & solar activity conditions.

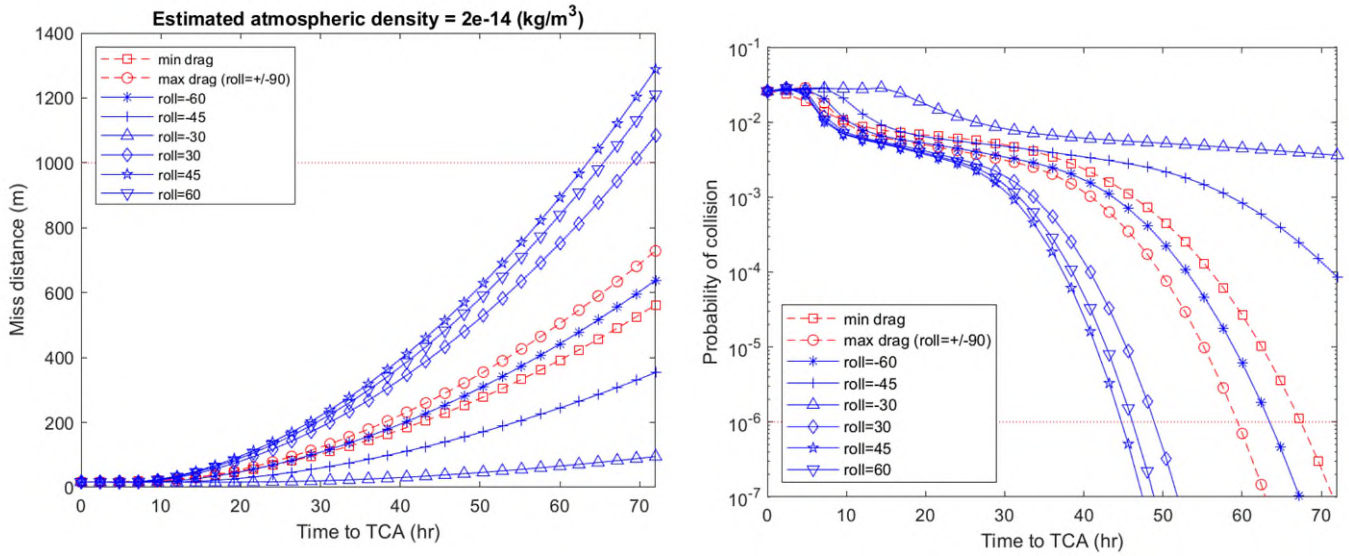

Figure 7: The miss-distance curves (left) and PoC curves (right) as functions of satellite orientation and time to TCA under medium geomagnetic & solar activity conditions.

Figure 6 shows the miss-distance and probability of collision (PoC) curves as functions of time to TCA and different satellite orientations, assuming low geomagnetic and solar activity conditions. The trade space plots indicate that neither the minimum nor maximum drag configurations can increase the miss distance to the 1000 m threshold or reduce the PoC to the 10^{-6} threshold within three days before TCA. Both configurations have almost similar effects, though the minimum drag configuration slightly improves the PoC. However, the plots also show that a 30-degree roll angle maneuver, which combines the effects of drag and solar radiation pressure (SRP), can reduce the PoC to the threshold within 68 hours, although the miss distance increases to only about half of the desired threshold. Figure 7 presents the results of OCAM for the same conjunction, assuming medium geomagnetic and solar activity conditions. In this case, both the minimum and maximum drag configurations can reduce the PoC to its threshold within 60 and

65 hours before TCA, respectively. The plots also indicate that a 45-degree roll angle maneuver effectively increases the miss distance and decreases the PoC, meeting their corresponding thresholds within 58 hours before TCA.

4 Conclusion

This study examined the feasibility of controlling perturbation forces due to aerodynamic drag and solar radiation pressure (SRP) through satellite orientation to enable propulsion-less collision avoidance maneuvers. The analysis accounted for drag-induced acceleration based on the exposed effective surface area and SRP-induced acceleration modeled as a combination of a blackbody absorber, a specular reflector, and a Lambertian diffuser. The maneuver's performance was evaluated by computing the resulting miss-distance and collision probability using conjunction data. The control algorithm required inputs such as the state vector from the CDM alert, cross-sectional areas of the primary satellite, surface reflectivity coefficients, and the atmospheric drag coefficient derived from solar activity levels or energy dissipation rate estimations. Case studies demonstrated that the Orientation-based Collision Avoidance Maneuver (OCAM) effectively enabled propulsion-less satellites to perform collision avoidance when sufficient warning time was available. The results showed that perturbation-based collision avoidance was effective for long warning times.

Acknowledgements

CSA acknowledges the contributions of DRDC in providing technical inputs during internal discussion on systems and operational constraints for implementation on the NEOSSat.

References

[1] D. Kessler, R. Reynold, and P. Ans-Meador, "TM 100-471 orbital debris environment for spacecraft designed to operate in low earth orbit," NASA JSC,, Houston, TX, Tech. Rep., 1989.

[2] M. Morton and T. Roberts, "Joint space operations center (jspoc) mission system (jms)," Defense Technica Information Center, Fort Belvoir, VA,, Tech. Rep., 2011, tR ADA550678.

[3] C. Bombardelli and J. Hernando-Ayuso, "Optimal impulsive collision avoidance in low earth orbit," *Journal of Guidance, Control, and Dynamics*, vol. 38, no. 2, pp. 217–225, 2015.

[4] F. Turco, C. Traub, S. Gaiber, J. Burgdorf, S. Klinkner, and S. Fasoulas, "An analysis tool for collision avoidance manoeuvres using aerodynamic drag," *Acta Astronautica*, vol. 211, pp. 116–129, 2023.

[5] D. Mishne and E. Edlerman, "Collision-avoidance maneuver of satellites using drag and solar radiatio pressure," *Journal of Guidance Control and Dynamics*, vol. 40, pp. 1191–1205, 2017.

[6] S. R. Omar and R. Bevilacqua, "Spacecraft collision avoidance using aerodynamic drag," *Journal of Guidance, Control, and Dynamics*, vol. 43, no. 3, pp. 567–573, 2020.

[7] C. Traub, S. Fasoulas, and G. H. Herdrich, "A planning tool for optimal three-dimensional formation flight maneuvers of satellites in vleo using aerodynamic lift and drag via yaw angle deviations," *Acta Astronautica*, vol. 198, pp. 135–151, 2022.

[8] A. M. N. Milani, A. and P. Farinella, *Non-gravitational Perturbations and Satellite Geodesy*. Taylor & Francis, 1987.

[9] L. Zardain, A. Farres, and A. Puig, "High-fidelity modeling and visualizing of solar radiation pressure: A framework for high-fidelity analysis," in *2020 AAS/AIAA Astrodynamics Specialist Conference*, August 2020.

[10] W. H. Clohessy and R. S. Wiltshire, "Terminal guidance system for satellite rendezvous," *Journal of Aerosapce Science*, vol. 27, no. 9, pp. 653–658, 1960.

[11] M. H. Kaplan, *Modern Spacecraft Dynamics and Control*. New York: Wiley, 1976.

[12] D. McKinley, "Maneuver planning for conjunction risk mitigation with ground-track control requirements," in *AAS/AIAA Spacecraft Mechanics Conference*, Galveston, TX, 2008.

[13] R. P. Patera, "General method for calculating satellite collision probability," *Journal of Guidance, Control, and Dynamics*, vol. 24, no. 4, pp. 716–722, 2001.

[14] G. Bollenbacher and J. D. Guptill, "Launch collision probability," NASA Glenn Research Center, OH, USA, Tech. Rep., 1999, no.: 19990079384.

[15] F. K. Chan, *Spacecraft Collision Probability*. El Segundo, California: The Aerospace Press, 2008.

[16] A. R. Hildebrand, E. F. Tedesco, K. A. Carroll, R. D. Cardinal, J. M. Matthews, and et al., "The near earth object surveillance satellite (neossat) mission will conduct an efficient space-based asteroid survey at low solar elongations," in *10th Asteroids, Comets, Meteors*, Baltimore, Maryland, July 14-18 2008.

[17] B. Wallace, S. R., S. M., H. A., and C. R., "The near earth object surveillance satellite: Mission status and ccd evolution after 18 months on orbit." in *Advanced Maui Optical & Space Surveillance (AMOS) Technologies*

Conference, Maui, Hawaii, 2014.

[18] S. R. and S. Thorsteinson, "Key findings from the neossat space–based ssa microsatellite mission," in *Advanced Maui Optical and Space Surveillance (AMOS) Technologies Conference*, Maui, Hawaii, 2018.

[19] Picone, J. M. and Hedin, A. E. and Drob, D. P. and Aikin, A. C.,'' NRLMSISE-00 empirical model of the atmosphere: Statistical comparisons and scientific issues''. Journal of Geophysical Research: Space Physics, Vol. 107, No. A12, SIA 15-1-SIA 15-16, 2008.